

# Laser-Induced Carbonization of Natural Organic Precursors for Flexible Electronics

Simon Delacroix, Huize Wang, Tobias Heil, and Volker Strauss\*

A precursor ink for carbon laser-patterning is developed using inexpensive, naturally abundant molecular compounds, namely citric acid and urea, and used to fine-print conductive carbon circuits on a flexible substrate. The precursor in the ink consists of organic nanoparticles obtained from the thermal treatment of citric acid and urea. This precursor is thoroughly characterized chemically and structurally. A simple recipe for the ink is then described for the creation of highly reproducible laser-patterned carbon structures on different substrates. Homogeneous  $\sim 20\ \mu\text{m}$  thick films are cast on different substrates and characterized before and after laser-carbonization. The carbon content of the final films is 97% and is of turbostratic graphitic nature. As reproducible laser-induced reactions depend on precise laser conditions, the influence of material properties, film thickness, and laser fluence are thoroughly analyzed. Films on three different substrates, namely aluminum sheets, silicon wafers, and polyethylene terephthalate (PET) are characterized by electrical impedance measurements. Electrical conductivities of up to  $5.21\ \text{S cm}^{-1}$  and maximum current densities of  $44\ \text{A cm}^{-2}$  are achieved, which proved applicable as fine carbon circuits on PET as a flexible substrate. This study opens a simple synthetic avenue to producing conductive circuit elements based on carbon.

## 1. Introduction

New fabrication methods for functional materials have driven the development of innovations and new products ever since. In fact, the industrial and commercial application and innovation of new products strongly depends on the identification of new processing methods. In particular, with respect to the processing and applicability of carbon nanomaterials (CNM), such as carbon nanotubes, graphene, and their relatives, new fabrication concepts are required.<sup>[1,2]</sup> Although CNMs find commercial applications in, for example, electrochemical sensors or energy storage, they still fall short in expectations in commercial electronics in general.<sup>[3,4]</sup> On top of that, it is a desirable goal to

replace toxic, expensive, or conflict materials with environmentally and socially more benign CNMs. Therefore, they are still considered promising candidates for a range of future applications in electronics, optoelectronics, or catalytic systems.


Laser-fabrication methods have been investigated as fast, energy-saving, low-cost, and precise material processing techniques in both science and industry and even a new “age of photon-driven materials manufacturing” has been prognosed.<sup>[5]</sup> In industry, laser-processing techniques are mainly used for cutting, welding, cladding, or surface processing.<sup>[6]</sup> It allows for high-precision materials modifications with unprecedented accuracy, not only spatially but also temporally, which is of particular interest for the manufacturing of future small-scale electronic and photonic products.

Also direct laser-induced materials synthesis has become an active field of research. For example, laser-induced ablation of graphite, discovered in the 1990s, is

commonly used for the targeted synthesis of CNMs.<sup>[7,8]</sup> High-power laser pulses hit a graphite target and create a carbon plasma above the surface, which reacts to crystalline nanocarbons. These laser-assisted synthesis methods differ from conventional thermal methods in the reaction time-scales. Heat transfer within micro- or milliseconds allows for reactions different to conventional heating methods.

Moreover, the precise spatial control with nano- to micrometer resolutions allows also for the fine patterning of materials. Generally, laser-patterning describes the micro-structuring of organic materials like polymers or plastics by evaporating material from their surface.<sup>[9]</sup> Directed 2D-film patterning by laser-induced material conversion evolved in the past years as a new synthetic fabrication method.<sup>[10]</sup> In particular, the uncomplicated access to laser-assisted patterning of graphene oxide and their relatives has given the field a significant push.<sup>[11–18]</sup> In most cases, graphene is produced by laser-induced reduction of graphene oxide (GO). Another famous laser-patternable material is polyimide (PI), which carbonizes at high temperatures.<sup>[19–21]</sup> Vast research efforts have been conducted on the characterization and application of laser-patterned GO or PI films.<sup>[22–24]</sup> However, the starting materials used are rather expensive and the modification of the resulting materials properties is limited since the starting materials are polymeric. Other materials could be used as precursor like paper or wood but without the possibility of choosing the initial substrate.<sup>[25]</sup>

Dr. S. Delacroix, H. Wang, Dr. T. Heil, Dr. V. Strauss  
Department of Colloid Chemistry  
Max-Planck-Institute of Colloids and Interfaces  
Am Mühlenberg 1, Potsdam 14476, Germany  
E-mail: volker.strauss@mpikg.mpg.de

 The ORCID identification number(s) for the author(s) of this article can be found under <https://doi.org/10.1002/aelm.202000463>.

© 2020 The Authors. Published by Wiley-VCH GmbH. This is an open access article under the terms of the Creative Commons Attribution License, which permits use, distribution and reproduction in any medium, provided the original work is properly cited.

DOI: 10.1002/aelm.202000463

A promising alternative starting material recently identified is phenolic resin,<sup>[26,27]</sup> but molecular starting materials are in fact rarely used. Most organic substances evaporate upon heat treatment with lasers due to the rapid heating to temperatures to well above 1000 °C in just a few milliseconds.

It has to be noted that laser-assisted material modification depends on several parameters, such as laser wavelength, power and energy density, absorptivity, and thermal conductivity of the active material and the substrate. The wavelength is critical for the interaction with the active material and the substrate. For example, a clear advantage of CO<sub>2</sub> lasers is the large penetration depth compared to short-wavelength lasers. A disadvantage, on the other hand, is the rather poor printing resolution due to the long wavelength. Power and energy density are governed by the spot size, the resolution, the laser power, and the scanning speed. The latter two are a result of the chemical and compositional properties of the materials. Therefore, a careful consideration of all these parameters has to be taken when applying laser treatment for materials modifications.

Recently, we identified an inexpensive molecular precursor system that was processed to an ink for laser-assisted carbonization to yield highly conductive carbon networks.<sup>[28]</sup> In brief, citric acid and urea are pre-carbonized in an annealing process at 300 °C. Inks produced from their reaction product in viscous solvents were applied onto different substrates and subsequently treated with a CO<sub>2</sub> laser to obtain fully carbonized films. Notably, this carbon laser-processing method does not require the use of catalysts. It became a question of scientific value what makes a precursor system laser-carbonizable as most organic substances evaporate in the high temperature reaction zone of a CO<sub>2</sub> laser.

We take this as a motivation to investigate the components of the inks and systematically investigate the laser-assisted carbonization process. First, we characterized the carbon precursor spectroscopically and microscopically in terms of composition and properties. We present a recipe for the production of a suitable ink and discuss the role of the laser-parameters to produce carbonized films on different substrates. The films were then characterized in terms of structure, composition, and electrical properties in order to make it applicable in thin film electronics.

## 2. Results and Discussion

### 2.1. Preparation of the Carbon Precursor

As demonstrated in earlier studies and in the literature, certain materials are suitable as precursors for laser-carbonization reactions. In contrast to conventional heating where carbonization is achieved within minutes or hours, laser-carbonization occurs on a time scale of milliseconds. On this fast time scale, even oxidation reactions by atmospheric oxygen are largely suppressed;<sup>[29,30]</sup> however, most organic materials, especially low-molecular-weight compounds evaporate without forming conductive carbon networks. It is still an open question what materials qualify for laser-carbonizations. In our studies, we found that a carbon precursor ink consists of three main components: the carbon-network forming agent (CNFA), the film-forming agent (FFA), and a solvent. In case of polymeric

precursors, the CNFA and FFA are combined in one structure. The FFA is an optional component for improving the wetting and processing properties of the ink.

In the first step, a precursor acting as a CNFA for the laser-assisted carbonization was prepared. A 1:1 mass mixture of citric acid and urea was annealed at 300 °C in a chamber oven producing a solid black foam referred to as CAU300. We refer to this process as pre-carbonization, due to the fact that the carbon content is increased from originally 33% in a 1:3 citric acid/urea mixture to 49% in the precursor for the laser process. The product was ground to a powder and further purified by a multistep washing process in H<sub>2</sub>O at 95 °C. The supernatant contains molecular intermediates, which are soluble in H<sub>2</sub>O. After two washing steps in H<sub>2</sub>O at 95 °C, the supernatant appears still brown but the apparent fluorescence turns from green to blue (Figure 1a). In the first washing step, unreacted low-molecular-weight intermediates were removed from the reaction product as shown in the <sup>1</sup>H-NMR patterns of the supernatants (Figure 1b). The dominant peaks at 5.39 and 9.84 originate from a green fluorophore: 4-hydroxy-1H-pyrrolo[3,4-c]pyridine-1,3,6(2H,5H)-trione (HPPT).<sup>[31]</sup> Only traces of these intermediates are found after the second washing step. The same supernatants were probed by UV-vis absorption spectroscopy. In the supernatant of the first washing step, a strong molecular absorption with maxima at 330 and 407 nm appear, which are assigned to the absorption of HPPT (Figure 1c). These absorption features appear as weak peaks in the supernatants of the subsequent washing steps. A closer look reveals a significant red-shift of these peaks after washing. For example, in the supernatants of washing steps 4 and 5, the second maximum appears red-shifted by 18 nm at 425 nm. The absorption features correlate to fluorescence in the visible. After the first washing step, the fluorescence intensity is significantly reduced and notably shifted to the blue (Figure S1, Supporting Information). A trailing absorption into the long wavelength region, between 500 and 900 nm, becomes more pronounced indicating the presence of dispersed particles. The low-intensity feature at 369 nm stems from the particles and may be assigned to an intra-particle charge-transfer band.

After five washing steps, the remaining mass amounts to ~85% of the original mass. This product, referred to as CAU300p (precipitate), was further characterized. Elemental analysis of CAU300p yields 49% C, 20% N, 3% H, and 28% O. The weight loss of CAU300 and CAU300p during heating of the sample in inert atmosphere (Figure 1g) was analyzed. For CAU300, a weight loss of ~3% in the low temperature regime <150 °C is ascribed to adsorbed H<sub>2</sub>O. At 343 °C, a large weight loss peak is assigned to HPPT, which amounts 15% of the sample. A further mass loss of 30% is noted in the temperature range between 300 and 800 °C, which is assigned to CAU300p. The residual mass at 1000 °C is 46% of the original weight. Notably, the thermogravimetric analysis of purified CAU300p shows an even more pronounced mass loss due to adsorbed H<sub>2</sub>O accounting for ~10% of the original weight. The residual mass is 40% of the original mass. This large decomposition temperature range and the rather large residual mass indicate polymerization at high temperatures.

After drying, the material appears as a light-weighted black powder that is finely dispersible in a range of solvents

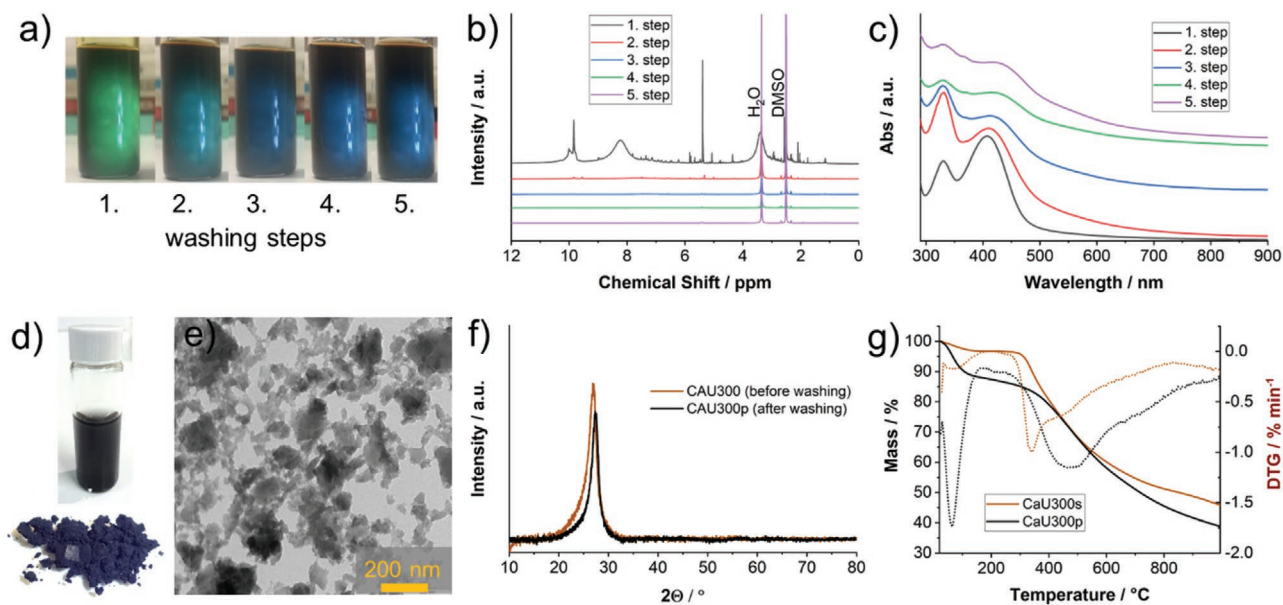


**Figure 1.** Characterization of CAU300p. a) Photographs depicting the aqueous supernatants after each washing step; b) <sup>1</sup>H-NMR patterns of the supernatants after each washing step in DMSO-d<sub>6</sub>; c) UV/vis absorption spectra of the supernatants after each washing step; d) photograph of purified CAU300p (bottom) and freshly dispersed in H<sub>2</sub>O; e) TEM image of CAU300p; f) powder X-ray diffraction patterns of CAU300 and CAU300p; g) thermogravimetric analysis of CAU300 and CAU300p.

(Figure S2, Supporting Information). Notably, after 24 h in H<sub>2</sub>O or methanol, the solid particles start to settle and the liquid phase turns weakly brown. This color change comes together with a blue fluorescence like the one observed during the last washing step of the process. In dimethyl sulfoxide (DMSO) and dimethylformamide (DMF), CAU300p appears well stabilized, as no solid phase was formed during centrifugation. This difference of dispersibility of CAU300p in water or DMSO is confirmed by dynamic light scattering (DLS) and transmission electron microscopy (TEM) measurements. At 20 °C, the dispersion of CAU300p in water or DMSO showed particles with mean sizes of  $240 \pm 12$  or  $5.5 \pm 3.5$  nm, respectively. The sample in the TEM image in Figure 1e was prepared from an aqueous dispersion of CAU300p and shows amorphous carbonaceous networks. Preparing the same sample from a DMSO solution, finely dispersed individual particles with sizes of 3–8 nm throughout the entire scanned area are seen (Figure S3, Supporting Information). We attribute this effect to the basicity of solvents like DMSO and DMF and their ability to stabilize acidic particles.

In the powder X-ray diffraction (XRD) pattern, a single sharp peak at  $26.9^\circ 2\theta$  (Figure 1f) is observed. The peak position indicates a typical graphitic (002) reflection corresponding to a lattice spacing of 3.33 Å. With regard to the peak width and according to the Scherrer-equation the crystallite size is  $\approx 5\text{--}6$  nm.

Taking the aforementioned results into concert, we assume an organic particulate structure of CAU300p. The sizes of these nanoparticles are on the order of a few nanometers as determined by TEM and DLS analysis. In most solvents, these nanoparticles aggregate to larger structures. In basic solvents such as DMSO or DMF, the particles are individually stabilized. Structurally, the sample is predominantly amorphous

with small crystalline domains. The green fluorophore HPPT formed during the thermal reaction is present in the product after annealing at 300 °C. Harsh washing conditions remove free HPPT from the product. However, as indicated by the presence of their absorption features in UV–vis spectroscopy, some HPPT may remain in CAU300p and may even be a main component. However, the strong red-shifts indicate a significant electronic interaction with other components. It seems likely that the insoluble CAU300p results as a thermal product from the decomposition or condensation of HPPT.

## 2.2. Preparation of the Carbon Ink and Printing

Our standard precursor ink is composed of CAU300p (48 wt%), polyvinylpyrrolidone 1000 (PVP) (8 wt%), and ethylene glycol (EtGly) (44 wt%). The first acts as a CNFA, the second as a FFA, and the last is a viscous, non-reactive solvent.

The films were prepared by doctor-blading the ink onto different substrates with a preset wet film thickness (i.e., 50–150 μm). The solvent was carefully evaporated at 80 °C on a precision hotplate. The mass loss during solvent evaporation was monitored for all substrates and found to be consistently  $44 \pm 2\%$  of the original mass, which accounts for the content of ethylene glycol. The final film thickness depends on the substrate and ranges between 15–40 μm resulting in areal mass loadings of 1–4 mg cm<sup>-2</sup> (Table 1). In Figure 2, a scanning electron micrograph (SEM) of the dried film cast from our standard CAU300p/PVP/EtGly precursor ink onto aluminum is presented. Upon evaporation of the solvent, cracks of <2 μm in the film evolve; however, these cracks are homogeneous across the entire film (Figure 2b, left). The Raman spectrum of these films shows two broad coalescing peaks at 1350 and 1590 cm<sup>-1</sup>



**Table 1.** Quantitative analysis of the precursor and carbonized films in terms of film thickness and mass density and results of the impedance measurements of laser-carbonized films on different substrates.

	Film thickness [ $\mu\text{m}$ ]	Areal mass density [ $\text{mg cm}^{-2}$ ]	Volumetric mass density [ $\text{mg cm}^{-2}$ ]	Fluence [ $\text{J cm}^{-2}$ ]	Mass loss [%]	Resistivity [ $\Omega \text{ cm}$ ]	Conductivity [ $\text{S cm}^{-1}$ ]	Current limit [mA]	Max. current density [ $\text{A cm}^{-2}$ ]
Al-1	19	1.29	677	7.1	43	0.23	4.38	3.6	38
Al-2	24	1.42	592	7.1	56	0.23	4.33	2.6	22
Al-3	19	1.31	704	3.8	18	—	—	—	—
Al-4	22	1.73	799	9.5	69	0.27	3.72	4.1	38
Si-1	22	3.13	1422	7.1	44	0.19	5.21	4.85	44
Si-2	38	3.87	1027	7.1	32	0.56	1.80	4.1	14
Si-3	25	3.16	1263	3.8	23	—	—	—	—
Si-4	22	3.10	1388	9.5	81	—	—	—	—
PET-1	20	0.95	467	7.1	76	0.74	1.35	1.10	10.9
PET-2	22	1.36	627	7.1	81	0.33	3.06	2.35	22
PET-3	24	1.69	706	3.8	10	—	—	—	—
PET-4	24	1.40	581	9.5	2554	—	—	—	—

indicating the presence of small graphitic domains (compare XRD in Figure 1).

After laser-treatment, the film appears with a metallic gleam, as shown in Figure 2b right. The SEM image in Figure 2c reveals a foam-like appearance with a hierarchical pore structure. The elemental analysis, tested by energy dispersive X-ray analysis (EDX) at seven different areas, yields a composition of  $97 \pm 0.2\%$  carbon and  $3 \pm 0.2\%$  oxygen (Figure S4, Supporting Information). The Raman spectrum of the laser-treated film (below) shows a pattern typically observed in turbostratic graphite samples.<sup>[32]</sup> Most prominent are two sets of peaks at 1336, 1564, and  $1602 \text{ cm}^{-1}$  and 2430, 2666, and  $2906 \text{ cm}^{-1}$ . The first set is composed of the D, G, and D' bands and the latter set is composed of the D+D', G', and D+G bands. The pronounced D and D' bands indicate the presence of defects in the graphitic lattice. The G' band was fit with a single Lorentzian with an FWHM of  $49 \text{ cm}^{-1}$  underlining the turbostratic nature of the graphitic network. To obtain a closer visual insight into the structure of the

laser-carbonized films, a TEM image of a fragment of the film is shown in Figure 2d. A crystalline, porous structure with pore sizes between a few tens and a few hundreds of nanometers is clearly visible. High-resolution TEM images and selected area electron diffraction (SAED) reveal lattices fringes characteristic for graphitic layers and a disordered, turbostratic crystal orientation (Figure S5, Supporting Information). The interplanar distance measured from the lattice fringes is around  $3.4 \text{ \AA}$ , which corresponds to the interlayer spacing of the graphitic samples.

A reaction mechanism of the laser-induced carbonization has been discussed earlier.<sup>[28,29]</sup> In brief, pre-carbonized organic nanoparticles containing significant amounts of functional groups are reduced in the hot reaction zone induced by the laser. Upon rapid cooling, these reduced nanoparticles form carbon-carbon bonds which results in a porous 3D-carbon network. Here, we would like to elucidate on the influence of some process parameters, like film thickness, absorptivity, laser fluence, and substrates.

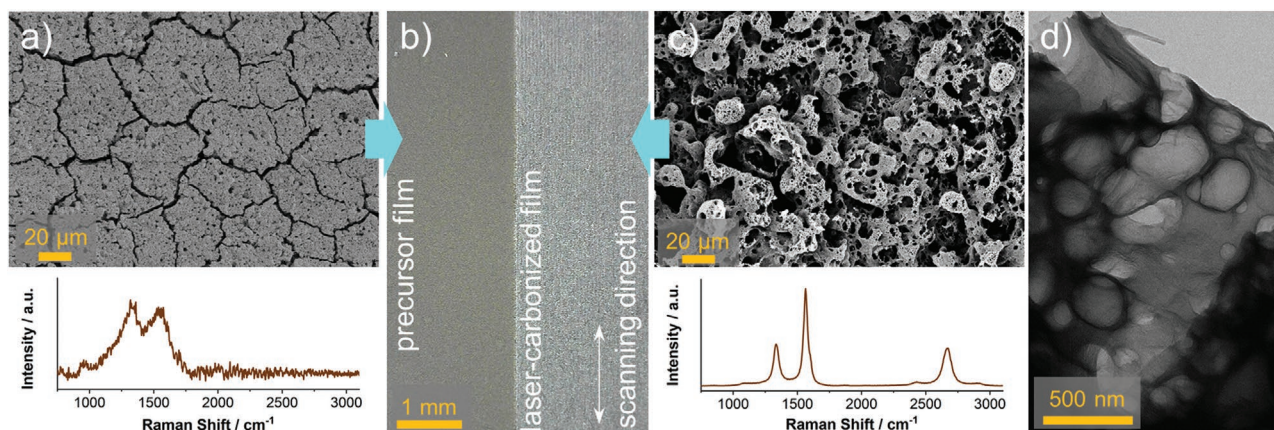


**Figure 2.** Characterization of films: doctor-bladed precursor films (CAU300p/PVP) and laser-carbonized films on aluminium sheets. a) SEM image of a CAU300p/PVP film and a corresponding Raman spectrum recorded upon excitation at 532 nm; b) low-magnification micrograph showing the precursor film on the left and the laser-carbonized film on the right; c) SEM image of a laser-carbonized CAU300p/PVP film and a corresponding Raman spectrum recorded upon excitation at 532 nm; d) TEM image of a fragment of the laser-carbonized CAU300p/PVP film.

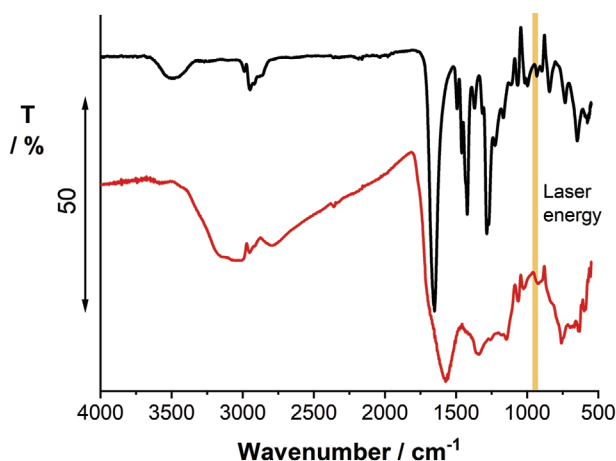


**Figure 3.** FT-IR spectra of PVP (black) and CAU300p (red). The orange line indicates the laser energy of the CO<sub>2</sub> laser corresponding to 10.6 μm.

A critical parameter for an effective heat transfer from the laser beam to the precursor film is the absorptivity of the laser energy (Figure 3). CAU300p shows a significant laser absorptivity at the characteristic laser energy while the absorptivity of PVP, the film forming agent, is negligible. High absorptivity leads to higher amount of heat transferred from the laser to the precursor material. Thus, for high extinction materials, a successful carbonization is achieved at lower energy input. The extinction coefficient of CAU300p at the laser wavelength 943 cm<sup>-1</sup> (10.6 μm) was experimentally determined by transmission Fourier-transform infra-red (FT-IR) absorption spectroscopy to be 0.56 L (g cm<sup>-1</sup>). Given a mass loading of, for example, 1.3 mg cm<sup>-2</sup> and a thickness of 20 μm, the laser light is absorbed to 81.3% by the film according to the Lambert–Beer law. For a smaller film thickness of, for example, 5 μm and the same volumetric mass loading, the laser light would only be absorbed by 34.2%. That implies that the initial energy density of 5.6 J cm<sup>-2</sup> is reduced to ≈50% after a penetration depth of 8 μm. It has to be taken into account that despite the successful laser-induced carbonization reaction, a significant fraction of precursor material evaporates due to heat absorption.

We tested the penetration depth on a thick precursor film with a mass loading of 4.04 mg cm<sup>-2</sup> prepared on a 11 × 25 cm quartz slide. The quartz slide acts as a flat and solid support for the precursor film during the micro-computer tomography (μ-CT) measurement. The images in Figure S6, Supporting Information, show slices of a μ-CT scan of the precursor film before (left) and after (right) laser treatment. From these scans, a film thickness of 75 μm for the precursor film was obtained. Using a manual digital micrometer (MDM), the thickness was measured to be 73 μm. For the laser-carbonized film, a thickness of 36 μm was obtained from the μ-CT scans, whereas the measurement with the MDM yielded 73 μm.

Considering the high mass loading of 4.04 mg cm<sup>-2</sup> on the quartz slide and the extinction coefficient of the precursor film (0.56 L (g·cm)<sup>-1</sup>), 92.4% of the laser energy is absorbed after a penetration depth of 35 μm (simplified by Lambert–Beer law). The laser-converted films are highly porous, as seen in the SEM images, and are expected to have a low contrast in the μ-CT scans. Therefore, we conclude that the 36 μm film observed

in the μ-CT scan in Figure S6, Supporting Information, on the right is the remaining unconverted precursor film. The laser-converted film is on top but cannot be seen in the tomograms.

Besides absorptivity, also the heat conductivity of the precursor film and the substrate has to be taken into account. The carbonization reaction from CAU300p to a conductive carbon network, as observed in Figure 2c, occurs in the hot plasma produced in the laser spot, but heat is dissipated across the film. High heat conductivity of the precursor or the substrate is expected to result in higher carbonization yield in the laser spot. To test the influence of the substrate, films with different thicknesses on aluminum sheets, silicon wafers, and polyethylene terephthalate (PET) were prepared by doctor blading. Aluminum sheets are flexible metal substrates with a high thermal conductivity (237 W (m·K)<sup>-1</sup>) and high transparency for the laser beam.<sup>[33]</sup> Silicon wafers are insulating substrates with high thermal conductivities (149 W (m·K)<sup>-1</sup>) and high reflectivity at the wavelength of the laser beam. In contrast, PET is a flexible substrate with a low thermal conductivity (0.24 W (m·K)<sup>-1</sup>) and a high absorptivity at the wavelength of the laser beam.

The energy density (fluence) of the laser beam onto the film is dependent on the laser parameters, such as effective output power, scanning speed, and resolution. Notably, these parameters are strongly instrument dependent. Based on the effective scanning speed and output power, we determined the effective fluences in our process to be in the range of 3–10 J cm<sup>-2</sup> (see Experimental Section). These values are slightly higher than typically used in laser-assisted micro and nanofabrication methods used for organic materials.<sup>[5]</sup>

The thicknesses of the applied films measured by MDM were in the range between 19 and 60 μm resulting in areal or volumetric mass densities between 1 and 4 mg cm<sup>-2</sup> or 500 and 1500 mg cm<sup>-3</sup> (Table 1). The different surface tension of the three chosen substrates causes different spreading across the area. For example, a higher volumetric mass density on Si-wafers is observed. Similar spreading properties were observed for aluminum or PET substrates. Notably, lower volumetric and higher areal mass densities were observed for thicker films. For all substrates, the areal mass density increases with higher film thickness. Application of the ink on PET results in thinner films, as spreading is facilitated by its low surface tension.

The films were irradiated with a CO<sub>2</sub> laser using different laser fluences. The mass loss scales with the film thickness and the effective energy density as shown in Table 1. Using the standard laser settings with an effective fluence of 7.1 J cm<sup>-2</sup> results in a mass loss of 43% on aluminum and 44% on Si-wafers. On PET, 76% mass loss is observed due to partial evaporation of the substrate. Higher fluence of, for example, 9.5 J cm<sup>-2</sup> causes larger amounts of material to evaporate during laser treatment. A special case is PET as a substrate, as high fluence leads to its evaporation. In fact, at an effective laser energy density of 9.5 J cm<sup>-2</sup>, a significant amount of PET evaporates as evidenced by a mass loss of >2000%.

We tested the electric properties of the laser-carbonized films on the different substrates. Impedance measurements of films with an area of 15 × 20 mm were performed and the serial resistance *R* (Ω) was determined from the impedance values. In the tested frequency range between 0.1 Hz and 100 kHz, probed at a constant current of 0.1 mA, the films performed like

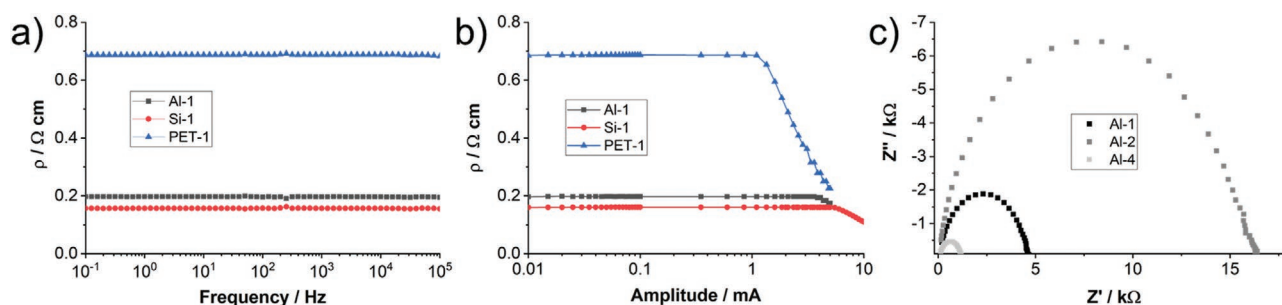


**Figure 4.** Resistance of the laser-carbonized CAU300p/PVP films in dependence of a) the frequency and b) the current amplitude obtained by impedance measurements on different substrates. c) Nyquist plots of laser-carbonized CAU300p/PVP films of different thicknesses on aluminium substrates.

ideal resistors (Figure 4a). From these measurements, sheet conductivities of  $1.3\text{--}5.2\text{ S cm}^{-1}$  were determined. Up to frequencies of 100 kHz, no notable skin effect, that is, increase of resistance at higher frequencies upon current density redistribution, was observed. Last, the maximum current densities for the films were tested, as an important characteristic of conductors in electric or electronic systems for the films on the three chosen substrates. The resistance of the films with respect to the applied electric current densities is plotted against the AC current amplitudes in Figure 4b. Up to a certain threshold, the resistance of the films scales constant with the applied current. In general, the maximum current densities scale with the sheet conductivities. Typical values for maximum current densities of, for example, copper wires are  $1 \times 10^5\text{ A cm}^{-2}$ .

In Table 1, the above discussed results of the impedance measurements are summarized and the complete set of data is shown in Figure S7, Supporting Information. Here, some interesting effects are observed. Using standard laser fluence of  $7.1\text{ J cm}^{-2}$ , the sheet conductivity on Si is significantly higher than on PET which could be attributed to the highest mass density. The conductivity is better if more precursor is reduced by the laser per square centimeter. For thicker films at this fluence, the sheet conductivity decreases, which is attributed to a larger unconverted layer. The lower layers remain unconverted and do not contribute to the overall conductivity of the film.

For aluminium, higher laser fluence leads to lower sheet conductivities, which are ascribed to higher material evaporation and thus lower resulting volumetric mass densities. In contrast to Si and PET as substrates, aluminum-supported films show good electric conductivity when irradiated with higher laser fluence of  $9.5\text{ J cm}^{-2}$ , which can be explained by the higher transmissivity of aluminum for the laser beam.

To acquire insights into the interfacial charge transport between the carbonized film and the substrate, we measured the impedance between the carbon film and the aluminium substrate. The charge transfer resistance is expressed in the difference of the two intersections at the  $Z'$ -axis of the semicircle in the Nyquist plot (Figure 5c). Clearly, the charge transfer resistance scales with the film thickness as it is reduced from 16 200 (Al-2) to 4600  $\Omega$  (Al-1). Larger amounts of unconverted precursors at the film/substrate interface cause higher charge-transfer resistance through the film. Notably, when using higher laser fluences for the carbonization, a smaller charge-transfer resistance of only 1084  $\Omega$  is achieved (Al-4).

To demonstrate the applicability of the laser-carbonized films as electronic conductors, we applied precursor films on a PET substrate by doctor blading an area of  $100 \times 50\text{ mm}$ . Conducting paths with a width of 0.5 mm as shown in Figure 5 were printed by the laser-patterning technique. The remaining material was removed by rinsing with deionized  $\text{H}_2\text{O}$ . Thereby, only the laser-carbonized material remained on the substrate. The conducting path form a circuit connecting a white LED with a 6 V power supply. On one side of the circuit, two strips with a distance of 5 mm were connected by sandwiching with a counter piece, which equally consisted of two 0.5 mm strips separated by 5 mm. Upon applying pressure to the crossover of the two conducting carbon strips, the circuit was closed and the white LED was lit.

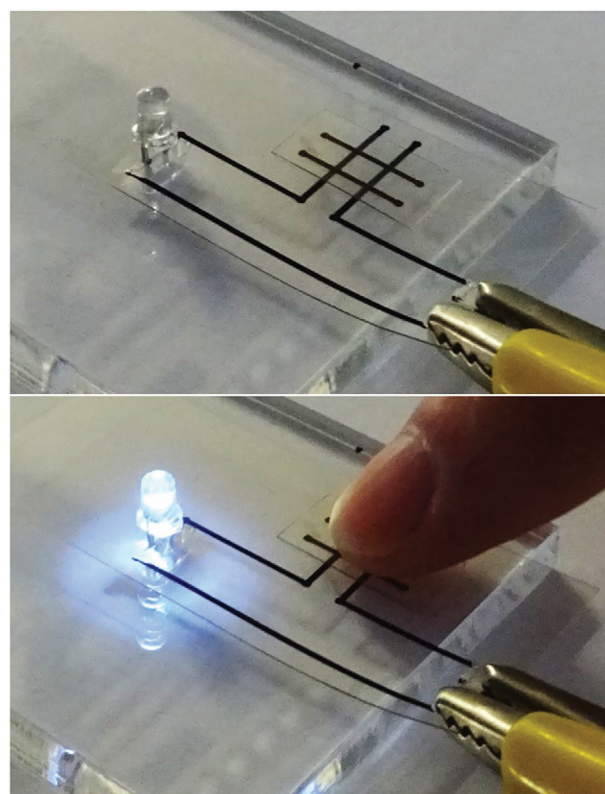


**Figure 5.** Photographs showing laser-patterned carbon conducting paths printed on a flexible, transparent PET substrate connecting an LED with a 6 V power supply being switched by applying pressure between the paths.



### 3. Conclusions

We have thoroughly investigated the laser-assisted carbonization reaction of inexpensive, small organic molecules, citric acid and urea. A pre-carbonization at 300 °C is necessary to form organic nanoparticles with an increased carbon content. We described a thorough workup and characterization of this pre-carbonized reaction product of citric acid and urea. A recipe for a precursor ink including these organic nanoparticles as carbon-network forming agents was introduced. Using this “standard ink,” we accomplished a full study on the reaction parameters of the laser-carbonization. Substrates, absorptivity, laser energy density, and film thickness were found to be highly critical parameters for the laser-carbonization process.

The results of this study help to gain an understanding of the criteria for laser-carbonizable materials. Printing fine patterns of conductive carbon on flexible substrates is possible, which makes this process generally attractive for flexible electronics. Fine-tuning of the carbon properties, like surface area and conductivity, will be essential for future applications and is currently under investigation.

### 4. Experimental Section

**Chemicals:** Citric acid (99.5% for analysis) and urea (Certified AR for analysis) were obtained from Fisher Scientific GmbH. Ethylene glycol ( $\geq 99.7\%$ , AnalaR Normapur) was obtained from VWR Chemicals. Polyvinylpyrrolidone (average mol wt. 10 000) was obtained from Sigma-Aldrich.

**Substrates:** Silicon wafers were obtained from MicroChemicals. Wafers used were either 4-in. boron-doped FZ-Si wafer, orientation (100), with a thickness of 0.5 mm and a generic resistivity of 3–100 k $\Omega$ cm or 4-in. FZ-Si wafer, orientation (100), with a thickness of 0.5 mm and a generic resistivity of 10–1000 k $\Omega$ cm. Aluminium foil used was 35  $\mu$ m thick. The PET substrate was Melinex sheets obtained from Plano GmbH.

**Preparation of CAU300p:** Citric acid and urea were thoroughly mixed in an alumina crucible or a glass crystallization dish. The vessel was covered with a lid to avoid spilling of the foaming reaction product, and to allow evaporation of evolving gases, a small opening under the lid was placed. The mixtures were annealed at 300 °C in a chamber oven for 2 h. After annealing, the black reaction product was retained and grinded to obtain a fine black powder. The mass of the product (CAU300) is 34% of the original mass of citric acid and urea. Then, CAU300 was dispersed in deionized H<sub>2</sub>O and stirred at 95 °C for 24 h. The dispersion was centrifuged to obtain a black precipitate and a brown supernatant. The supernatant was removed and the washing process was repeated four times. After the last washing step, the precipitate was dried to obtain CAU300p, which amounted  $\approx 85\%$  of the original mass.

**Preparation of the Precursor Films:** PVP was dissolved in EtGly to obtain a 200 mg mL<sup>-1</sup> solution (PVP/EtGly). CAU300p was then added and stirred for 24 h to obtain a 1 g L<sup>-1</sup> dispersion. The resulting slurry was used as a carbon precursor ink. A drop of the ink was applied onto the substrate and the ink was doctor bladed with different wet thicknesses between 50 and 150  $\mu$ m. Ethylene glycol was then evaporated at 80 °C on a precision hotplate (PZ2860-SR, Gestigkeit GmbH) to obtain the final films with thicknesses between 15 and 40  $\mu$ m.

**Laser-Assisted Carbonization:** Laser-assisted carbonization was conducted with a high-precision laser engraver setup (Speedy 100, Trotec) equipped with a 60 W CO<sub>2</sub> laser. Focusing was achieved with a 2.5 inch focus lens providing a focal depth of  $\approx 3$  mm and a focus diameter of 170  $\mu$ m. The center wavelength of the laser was 10.6  $\pm$  0.03  $\mu$ m. The scanning speed  $v$ , generically given in %, was converted

into s cm<sup>-2</sup>. The resulting energy input per area (or fluence) onto the film is given by

$$F = P \times v = P \times \frac{t}{A} \quad (1)$$

where  $P$  is the effective power. The laser settings (speed, power, and resolution) were adjusted to meet the requirements of the precursor film and the substrate prior to the experiments (Figure S8, Supporting Information). Typically, 10% power, 20% speed, and a resolution of 1000 dpi were chosen, for which resulted a fluence of  $F = 7.1 \frac{J}{cm^2}$ . The effective output power of the laser was measured with a Solo 2 (Gentec Electro-Optics) power meter.

**Instrumental:** Scanning electron microscopy was performed on a Zeiss LEO 1550-Gemini system (acceleration voltage: 3 to 10 kV). An Oxford Instruments X-MAX 80 mm<sup>2</sup> detector was used to collect the SEM-EDX data. Transmission electron microscopy was performed using an EM 912 Omega from Zeiss operating at 120 kV. To prepare the TEM samples, the carbon material was dispersed in methanol by sonication for 10 min and applying 5  $\mu$ L droplets of the dispersion on a carbon-coated copper TEM grid and drying at room temperature. Thermogravimetric analysis was performed using a Thermo Microbalance TG 209 F1 Libra (Netzsch, Selb, Germany). A platinum crucible was used for the measurement of  $10 \pm 1$  mg of samples in a nitrogen flow of 20 mL min<sup>-1</sup> and a purge flow of 20 mL min<sup>-1</sup> at a heating rate of 10 K min<sup>-1</sup>. Elemental analysis was performed with a vario MICRO cube CHNOS elemental analyzer (Elementar Analysensysteme GmbH). The elements were detected with a thermal conductivity detector (TCD) for C, H, N, and O and an infrared (IR) detector for sulfur. UV–vis–NIR absorption measurements were performed with a Specord 210 plus from Analytik Jena using 10 mm quartz cuvettes. Fluorescence measurements were performed with a Fluoromax 4 from Horiba. Fourier-transform infrared measurements were performed using a Nicolet iS 5 FT-IR-spectrometer in conjunction with an iD5 ATR unit from ThermoFisher Scientific. Extinction coefficients were determined by measuring a series of transmission infra-red absorption spectra with known concentrations in the range between 1.6 and 7.8 g L<sup>-1</sup> pressed into KBr pellets. The absorbance was plotted against the concentration and the extinction coefficients were determined from the slope of the fitting curve. Raman spectra were obtained with a confocal Raman Microscope (alpha300, WITec, Germany) equipped with a piezo-scanner (P-500, Physik Instrumente, Karlsruhe, Germany). The laser,  $\lambda = 532$  or 785 nm, was focused on the samples through a 20 $\times$  objective. The laser power on the sample was set to 1.0 mW. The spectra were acquired using a thermoelectrically cooled CCD detector (DU401A-BV, Andor, Belfast, North Ireland) behind a 600 g mm<sup>-1</sup> grating spectrograph (UHTS 300, WITec, Ulm, Germany) with a spectral resolution of 3 cm<sup>-1</sup>. The WITec Control Five software (Version 5.2, WITec, Ulm, Germany) was used for measurement setup. X-ray diffraction was performed on a Bruker D8 Advance diffractometer in the Bragg–Brentano mode at the Cu K $\alpha$  wavelength. Nuclear-magnetic resonance spectroscopy was measured on a 400 MHz Bruker Ascend400. Impedance measurements were performed on a Solartron 1287 potentiostat in combination with a SI 1260 impedance unit. For frequency measurements, the current was kept constant at 0.1 mA, and for current sweeps, a frequency of 1000 Hz was used. Dynamic light scattering was performed on a Zetasizer Nano ZS from Malvern Panalytical at 20 °C (He-Ne laser 633 nm). Micro-computer tomography ( $\mu$ -CT) was performed on a EasyTom 160 3D Tomography System from RXSolutions. The scans were performed with a sealed microfocus tube equipped with a tungsten filament and a flat panel detector with a CsI (caesium iodide) scintillator. The wavelength of the generated X-rays was 1.5418 Å (Cu K $\alpha$ ).

**Associated Content:** General and supplementary information on synthesis and characterization. Fluorescence spectroscopy of the supernatants during the washing process, photographs of suspensions, transmission electron micrographs, energy-dispersive X-ray analysis, micro-computer tomography measurements, and electrical impedance measurements.

## Supporting Information

Supporting Information is available from the Wiley Online Library or from the author.

## Acknowledgements

The authors thankfully acknowledge the permanent educational and the financial support from the Max Planck Society and the Fonds financial support from the Fonds der Chemischen Industrie. The authors thank Daniel Werner for performing micro-CT measurements micro-CT measurements, Heike Runge and Rona Pitschke for Microscopy, Antje Völkel for elemental analysis.

## Conflict of Interest

The authors declare no conflict of interest.

## Keywords

carbon circuits, electrical impedance, flexible electronics, laser carbonization, laser patterning

Received: April 30, 2020

Published online: September 3, 2020

- 
- [1] M. F. L. De Volder, S. H. Tawfick, R. H. Baughman, A. J. Hart, *Science* **2013**, 339, 535.
- [2] R. Rao, C. L. Pint, A. E. Islam, R. S. Weatherup, S. Hofmann, E. R. Meshot, F. Wu, C. Zhou, N. Dee, P. B. Amama, J. Carpena-Nuñez, W. Shi, D. L. Plata, E. S. Penev, B. I. Yakobson, P. B. Balbuena, C. Bichara, D. N. Futaba, S. Noda, H. Shin, K. S. Kim, B. Simard, F. Mirri, M. Pasquali, F. Fornasiero, E. I. Kauppinen, M. Arnold, B. A. Cola, P. Nikolaev, S. Arepalli, et al., *ACS Nano* **2018**, 12, 11756.
- [3] *Nanocarbons for Advanced Energy Conversion* (Ed: X. Feng), Wiley-VCH Verlag, Weinheim **2015**.
- [4] *Nanocarbons for Electroanalysis* (Eds: S. Szunerits, R. Boukherroub, A. Downard, J.-J. Zhu), John Wiley & Sons, Chichester, UK **2017**.
- [5] *Laser-Assisted Fabrication of Materials* (Eds: J. D. Majumdar, I. Manna), Springer Series in Materials Science, Vol. 167, Springer, Berlin **2013**.
- [6] U. S. Springe, *Laser Fabrication and Machining of Materials*, Springer, Boston, MA **2008**.
- [7] Y. Zhang, H. Gu, S. Iijima, *Appl. Phys. Lett.* **1998**, 73, 3827.
- [8] Y. van de Burgt, *J. Laser Appl.* **2014**, 26, 032001.
- [9] W. Pflöging, R. Kohler, I. Südmeyer, M. Rohde, in *Laser-Assisted Fabrication of Materials* (Eds: J. D. Majumdar, I. Manna), **2013**, pp. 319–374.
- [10] D. Zhang, B. Gökce, S. Barcikowski, *Chem. Rev.* **2017**, 117, 3990.
- [11] R. Kumar, R. K. Singh, D. P. Singh, E. Joanni, R. M. Yadav, S. A. Moshkalev, *Coord. Chem. Rev.* **2017**, 342, 34.
- [12] V. Strong, S. Dubin, M. F. El-Kady, A. Lech, Y. Wang, B. H. Weiller, R. B. Kaner, *ACS Nano* **2012**, 6, 1395.
- [13] R. Trusovas, K. Ratautas, G. Račiukaitis, J. Barkauskas, I. Stankevičienė, G. Niaura, R. Mažeikienė, *Carbon N. Y.* **2013**, 52, 574.
- [14] W. Gao, N. Singh, L. Song, Z. Liu, A. L. M. Reddy, L. Ci, R. Vajtai, Q. Zhang, B. Wei, P. M. Ajayan, *Nat. Nanotechnol.* **2011**, 6, 496.
- [15] D. A. Sokolov, C. M. Rouleau, D. B. Geohegan, T. M. Orlando, *Carbon N. Y.* **2013**, 53, 81.
- [16] D. A. Sokolov, K. R. Shepperd, T. M. Orlando, *J. Phys. Chem. Lett.* **2010**, 1, 2633.
- [17] E. Ghoniem, S. Mori, A. Abdel-Moniem, *J. Power Sources* **2016**, 324, 272.
- [18] F. Wang, K. Wang, B. Zheng, X. Dong, X. Mei, J. Lv, W. Duan, W. Wang, *Mater. Technol.* **2018**, 33, 340.
- [19] A. Bürger, E. Fitzer, M. Heym, B. Terwiesch, *Carbon N. Y.* **1975**, 13, 149.
- [20] M. Inagaki, S. Harada, T. Sato, T. Nakajima, Y. Horino, K. Morita, *Carbon N. Y.* **1989**, 27, 253.
- [21] J. Lin, Z. Peng, Y. Liu, F. Ruiz-Zepeda, R. Ye, E. L. G. Samuel, M. J. Yacaman, B. I. Yakobson, J. M. Tour, *Nat. Commun.* **2014**, 5, 5714.
- [22] R. Ye, D. K. James, J. M. Tour, *Adv. Mater.* **2019**, 31, 1803621.
- [23] J. Bin In, B. Hsia, J.-H. Yoo, S. Hyun, C. Carraro, R. Maboudian, C. P. Grigoropoulos, *Carbon N. Y.* **2015**, 83, 144.
- [24] R. Ye, D. K. James, J. M. Tour, *Acc. Chem. Res.* **2018**, 51, 1609.
- [25] Y. Chyan, R. Ye, Y. Li, S. P. Singh, C. J. Arnusch, J. M. Tour, *ACS Nano* **2018**, 12, 2176.
- [26] M. Sopronyi, F. Sima, C. Vaulot, L. Delmotte, A. Bahouka, C. Matei Ghimbeu, *Sci. Rep.* **2016**, 6, 39617.
- [27] J. Liu, L. Zhang, C. Yang, S. Tao, *J. Mater. Chem. A* **2019**, 7, 21168.
- [28] V. Strauss, K. Marsh, M. D. Kowal, M. F. El-Kady, R. B. Kaner, *Adv. Mater.* **2018**, 30, 1704449.
- [29] V. Strauss, M. Anderson, C. L. Turner, R. B. Kaner, *Mater. Today Energy* **2019**, 11, 114.
- [30] Y. Li, D. X. Luong, J. Zhang, Y. R. Tarkunde, C. Kittrell, F. Sargunary, Y. Ji, C. J. Arnusch, J. M. Tour, *Adv. Mater.* **2017**, 29, 1700496.
- [31] W. Kasprzyk, T. Świergosz, S. Bednarz, K. Walas, N. V. Bashmakova, D. Bogdał, *Nanoscale* **2018**, 10, 13889.
- [32] L. M. Malard, M. a. Pimenta, G. Dresselhaus, M. S. Dresselhaus, *Phys. Rep.* **2009**, 473, 51.
- [33] L. Cui, H. J. Butler, P. L. Martin-Hirsch, F. L. Martin, *Anal. Methods* **2016**, 8, 481.